WILEY-VCH

RESEARCH ARTICLE

Zn (II)-doped cesium copper halide nanocrystals with high quantum yield and colloidal stability for high-resolution X-ray Imaging

Kang Qu, Yangbin Lu, Peng Ran, Kun Wang, Nan Zhang, Kaiyu Xia, Hongyan Zhang, Xiaodong Pi, Hanlin Hu, Yang (Michael) Yang, Qingquan He, Jun Yin* and Jun Pan*

K. Qu, Y. Lu, N. Zhang, K. Xia, H. Zhang, Q. He, J. Pan
College of Materials Science and Engineering
Zhejiang University of Technology
Hangzhou 310014, China
E-mail: panjun0123@zjut.edu.cn
J. Yin
Department of Applied Physics
The Hong Kong Polytechnic University
Kowloon 999077 Hong Kong, China
E-mail: jun.yin@polyu.edu.hk
P. Ran, Y. (M.) Yang
State Key Laboratory of Modern Optical Instrumentation
Institute for Advanced Photonics
College of Optical Science and Engineering
Zhejiang University
Hangzhou 310027, China
K. Wang, X. Pi
State Key Laboratory of Silicon Materials & School of Materials Science and Engineering
Zhejiang University
Hangzhou 310027, China
H. Hu
Hoffmann Institute of Advanced Materials
Shenzhen Polytechnic
Shenzhen 518055, China

Supporting information for this article is given via a link at the end of the document.

Abstract: Scintillators are essential for high-energy radiation detection in a variety of potential applications. However, due to complex fabrication processes and nanocrystal homogeneity, conventional scintillators are challenging to meet the need for cost-effective, environmentally friendly, and flexible X-ray detection. Here, monodisperse nanocrystals (NCs) with small grain size and colloidal stability were obtained by adjusting the doping concentration of Zn^{2+} ions and controlling the morphology uniformity of $Cs_3Cu_2I_5$ NCs. The photoluminescence quantum yield (PLQY) for the optimal doping concentration was as high as 92.8%, which is a 28.5% improvement compared to non-doped NCs. Density functional theory calculations reveal that the Zn^{2+} dopant inclines to occupy Cu sites and the I-rich condition suppresses the formation of I vacancy, enriching the excited electron density at the band-edge to enhance the self-trapped exciton emission. Moreover, high luminescence performance and flexible X-ray scintillator films were prepared using Zn^{2+}-doped $Cs_3Cu_2I_5$ NCs, with a spatial resolution of up to 15.7 lp/mm. This work provides an effective strategy for the development of environmentally friendly, low-cost, and efficient blue-emitting 0D all-inorganic metal halides, as well as shows great potential for high-performance flexible lead-free and low-toxicity X-ray detector applications.

Introduction

X-ray detectors have a wide range of applications in medicine and industry. Metal halide perovskites, which are the new generation of semiconductor materials, have the advantage of a large X-ray absorption coefficient, fast X-ray photoresponse, and adjustable bandgap, thereby exhibiting extraordinary X-ray detection performance.[1] To date, high-quality lead-based perovskite single crystals have demonstrated ultra-high detection performance. However, they are limited by their current shortcomings, including the toxicity of lead, chemical instability, inherent brittleness of bulk crystals, and their high-temperature fabrication and complex processes.[2] Therefore, the development of low-cost, environmentally friendly, flexible X-ray detectors and novel scintillators still remain a challenge.

Owing to the high emission stability, low self-absorption, soft lattice, unique self-trapped exciton emission (STE),[3] and relatively low toxicity and earth-abundant composition, lead-free copper-based halide $Cs_3Cu_2I_5$ nanocrystals (NCs) have attracted extensive attention in the field of optoelectronics,[4] such as electroluminescent Light-Emitting Diode (LED) devices,[5] ultraviolet (UV) photodetectors,[6] X-ray imaging,[7] and anti-counterfeiting technology.[8]

Although progress has been made in the synthesis and application of $Cs_3Cu_2I_5$ NCs,[9] the insufficient synthesis reaction and difficulty in controlling the crystal size, morphology, and uniformity of $Cs_3Cu_2I_5$ NCs still remain the main obstacles

hindering device performance and fundamental research.[10] Metal ion doping is an effective way to tune the structure and optoelectronic properties of materials, which is frequently reported for lead-based perovskite systems.[11] However, relevant theoretical and experimental developments are missing for the cesium copper halide materials, which need to be explored and improved through in-depth research.

Considering the ionic radius and spatial configuration of Cu^+, Zn^{2+} was proved to be an excellent dopant.[12] In particular, zinc is economical and environmentally friendly compared to other studied elements that have been used for doping $Cs_3Cu_2I_5$ (such as cadmium, thallium, and indium).[13] Zn^{2+} cations are expected to stabilize the crystalline structure,[14] improve the photoluminescence (PL) performance, and maintain the low toxicity of $Cs_3Cu_2I_5$ NCs. These advantages have inspired us to incorporate ZnI_2 into $Cs_3Cu_2I_5$ NCs for the realization of excellent optoelectronic properties.

Herein, we proposed an approach by incorporating heterovalent Zn^{2+} cations into $Cs_3Cu_2I_5$ NCs, forming a series of $Cs_3Cu_2I_5$: Zn NCs ($0 \le Zn/Cu \le 1$), which resulted in a progressive lattice contraction but without changing the crystalline forms of the $Cs_3Cu_2I_5$ NCs. The results show that Zn^{2+} doping can tune the growth kinetics balance of NCs to control their size morphology of NCs. Notably, the as-prepared NCs exhibited a high phase purity, a PLQY of up to 92.8%, and an excellent stability under ambient conditions. Finally, we presented the high luminescence performance and flexible X-ray scintillator films based on Zn^{2+}-doped $Cs_3Cu_2I_5$ NCs with a spatial resolution as high as 15.7 lp/mm.

Results and Discussion

Colloidal $Cs_3Cu_2I_5$ NCs were synthesized using a simple hot injection method by directly adding zinc iodide salt to the precursor, as shown in the schematic diagram in Figure 1a (see details in the experimental section).[15] It is worth mentioning that the addition of ZnI_2 is essential for high PLQYs, which is the main difference compared to the recently reported synthesis method of $Cs_3Cu_2I_5$ NCs.[13a] In addition to the addition of ZnI_2, we also found that high injection temperatures and the cesium source injection volume are favorable for high PLQYs. During the synthesis of the Zn^{2+}-doped $Cs_3Cu_2I_5$ NCs, the injection temperature and added volume of ZnI_2 were the two factors that effectively controlled the NC morphology.

X-ray diffraction (XRD) was used to investigate the crystalline structure of the Zn^{2+}-doped $Cs_3Cu_2I_5$ NCs. The characteristic diffraction peaks at 24.0°, 25.6°, and 26.3° assigned to the (122), (320) and (222) planes, respectively, matching with standard $Cs_3Cu_2I_5$ PXRD data (JCPDS No. 79-0333). This was a strong indication of the formation of host $Cs_3Cu_2I_5$ NCs (Figure 1b). Furthermore, the partially enlarged XRD pattern (the right in Figure 1b) showed that the diffraction peak positions of the (004) plane gradually shifted to higher angles without introducing any additional peaks as the Zn/Cu ratio increased. The red shift indicated that the incorporation of zinc ions maintained the crystalline phase of $Cs_3Cu_2I_5$ NCs, but induced lattice shrinkage. Since the ionic radius of Zn^{2+} (74 pm) is slightly smaller than that of Cu^+ (77 pm),[12] the decreased lattice parameter implied that Zn^{2+} cations had partially replaced the Cu^+ cations, rather than being located at interstitial sites.

High-temperature synthesis generally favors the formation of high-quality crystals with fewer defects. To verify the advantages of high-temperature synthesis, monodisperse $Cs_3Cu_2I_5$ NCs were synthesized at 70 °C, 150 °C, and 180 °C (where the feed molar ratio of Zn/Cu was 0.75 and the feed molar ratio of Cs/Cu was 1.0). Transmission electronic microscopy (TEM) was used to characterize the morphologies and composition of the obtained NCs, The TEM results showed that the synthesis at low temperature (70 °C) tended to produce more crystalline defects, in contrast to more uniform crystalline growth at high-temperature synthesis conditions. For a synthesis temperature of 180 °C, the resulting $Cs_3Cu_2I_5$ NCs were cubic-shaped, and the average size was reduced to a minimum value of approximately 16.5 nm (Figure S1). However, when the synthesis temperature was larger than 180 °C, CuI tended to precipitate in the precursor solution prior to injection, which could greatly reduce the yield of the final synthesized nanocrystals. Meanwhile, the nanocrystal size could be large and uncontrollable with no addition of ZnI_2 precursor, which is not conducive to a stable existence in the solvent. Thus, the effect of ZnI_2 in inhibiting the growth of $Cs_3Cu_2I_5$ NCs at high temperatures has been well demonstrated.

After fixing the reaction temperature at 180 °C, different zinc doping concentrations were investigated. For Zn/Cu feed ratios less than 0.5, the nanocrystals are spherical (Figure 1c) with an average diameter of 23.6 nm (Figure S2a), which is similar to those synthesized at low temperature (Figure S1a). As shown in Figure S3a, the nanocrystals tended to agglomerate in the solvent as time progressed, thereby losing their monodisperse properties. When the Zn/Cu ratio reached 0.75, the monodisperse crystalline growth was inhibited and the morphology was uniformly cubic-shaped with an average diameter of 17.8 nm (Figure 1d, Figure S2b). Notably, there was no distinct change in the morphology and nanocrystals size after 10 days (Figure S3c), indicating that the cubic shaped nanocrystals of $Cs_3Cu_2I_5$ experienced good morphological stability. Figure 1e presents a high-resolution TEM (HRTEM) image of a single nanocrystal, and its corresponding fast Fourier-transform (FFT) pattern is shown in Figure 1f. The clear lattice diffraction streaks indicate a high crystalline quality of the single crystal with no apparent defects. The lattice spacing of 0.338 nm is consistent with the (222) plane of $Cs_3Cu_2I_5$, and the same (222) plane detected in the FFT pattern corresponds to the strongest peak in the XRD pattern.

With the addition of ZnI_2, the halogen vacancy defects on the surface of the nanocrystals could be passivated by the additional iodide ions. However, when the Zn/Cu feed ratio was increased to 1.0, the appearance of brick-like nanocrystals was observed (Figure 1g). As shown in Figure S2c, S2d, the average length is 36.5 nm and the average width is 20.7 nm. We also observed a self-assembly behavior of the brick-like nanocrystals to form nanowires. TEM images of the results from the self-assembling process, on the second and third days, are shown in Figures. 1h and 1i, respectively. The lattice spacing of 0.304 nm in Figure 1j corresponds to the (002) plane of $CsCu_2I_3$ (JCPDS No.77−0069; Space group, Cmcm), which further confirms the formation of $CsCu_2I_3$ NWs.[16] Grazing incident wide angle X-ray scattering (GIWAXS) has also been performed to examine the crystal structure of $Cs_3Cu_2I_5$ NCs. As a result, the transition from scattering rings to scattering spots indirectly demonstrated an increase in the dimensionality from 0D to 1D of the nanocrystals with higher order. (Figure S4).

Although ZnI_2 could passivate the nanocrystal surface, an excess content of zinc led to an enhanced extraction of Cs^+ ions.[17] In addition, ZnI_2 could also react with the surface ligand OAm. Hence, we further adjusted the OAm-to-OA ratio in the reaction system (Figure S5). The formation of $CsCu_2I_3$ was closely related to the coordination of copper ions with OAm[18]. Low doses of OAm could promote the formation of $CsCu_2I_3$ at high temperatures. Therefore, the formation of $CsCu_2I_3$ NWs was more favorable than the formation of $Cs_3Cu_2I_5$ NCs by the addition of a high content of ZnI_2 precursors. This transformation was similar to the previous results by Shi et al. They treated the $Cs_3Cu_2I_5$ NCs film with moisture, and the blue emission of $Cs_3Cu_2I_5$ NCs gradually evolved to the yellow emission of $CsCu_2I_3$ NWs under UV excitation ($Cs_3Cu_2I_5 \rightarrow CsCu_2I_3 + CsI$).[19] Thus, the addition of ZnI_2 was found to play an important role in the morphological control of $Cs_3Cu_2I_5$ NCs.

Figures 1k-o display the elemental mapping of the optimal Zn^{2+}-doped $Cs_3Cu_2I_5$ NCs (with a Zn/Cu feed ratio of 0.75). All the corresponding mapping images of Cs, Cu, I, and Zn in the Zn^{2+}-doped nanocrystals are covered with TEM images, indicating the presence of Zn^{2+} in the $Cs_3Cu_2I_5$ NCs. The same results were obtained for the self-assembled $CsCu_2I_3$ NWs, revealing that Zn^{2+} ions were easily doped and stably present in the Cs-Cu-I system (Figure S6). Moreover, the exact dopant content in the nanocrystals was quantified using inductively coupled plasma-optical emission spectrometry (ICP-OES). The ICP-OES results confirmed the successful incorporation of Zn^{2+} dopants into the $Cs_3Cu_2I_5$ host with a dopant concentration of 17% (Table S1).

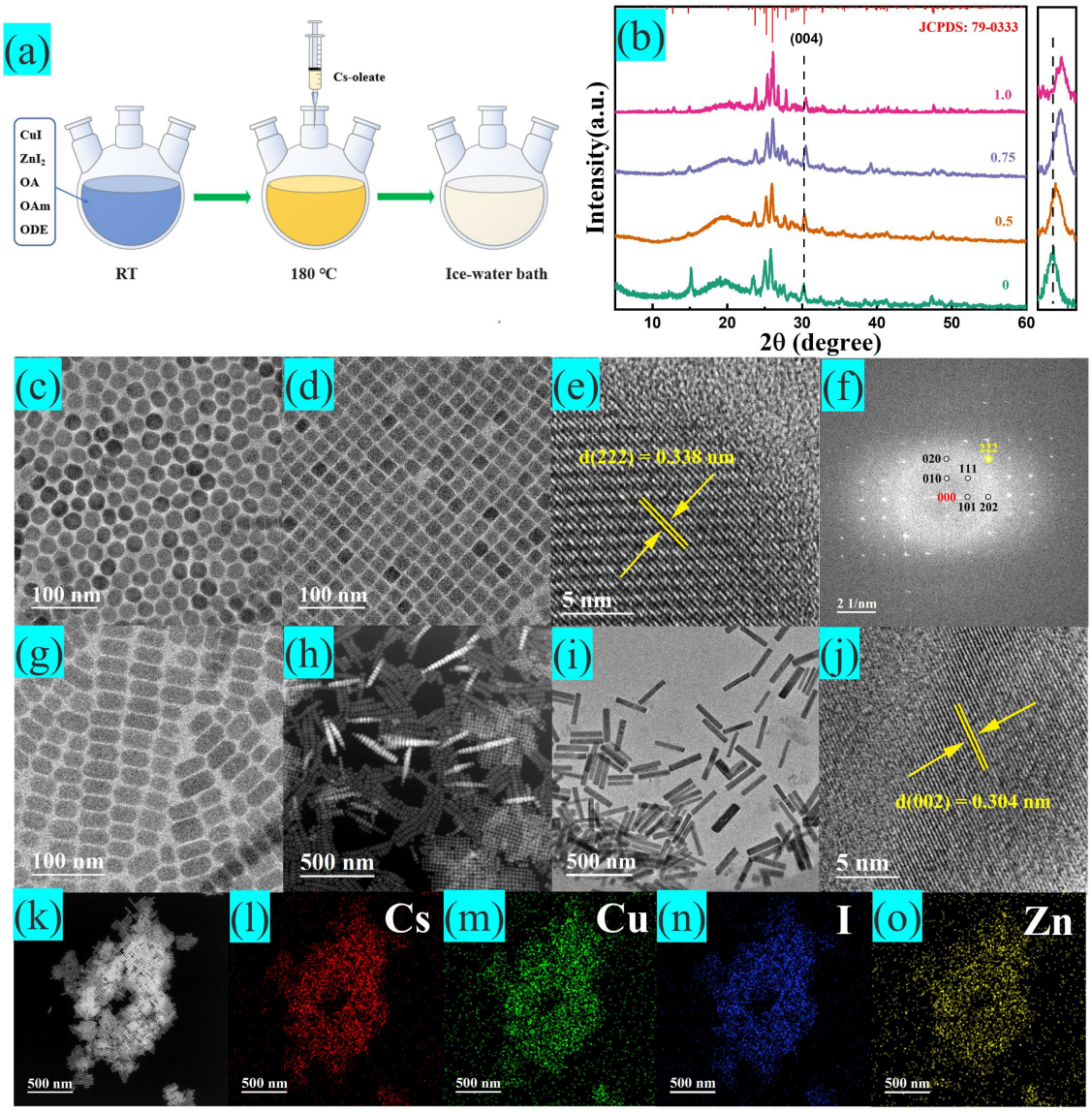

Figure 1. (a) Schematic diagram for synthesis of Zn^{2+}-doped $Cs_3Cu_2I_5$ NCs. (b) XRD patterns of $Cs_3Cu_2I_5$ NCs with Zn/Cu ratios of 0.5, 0.75, 1. (c, d) TEM images of different Shape of $Cs_3Cu_2I_5$ NCs. (e, f) High-resolution TEM image of cubic nanocrystal and the corresponding FFT images. (g-j) Self-assembly of $Cs_3Cu_2I_5$ NCs to $CsCu_2I_3$ NWs. (k-o) HAADF-STEM image of $Cs_3Cu_2I_5$ NCs with Zn/Cu ratios of 0.75.

The $Cs_3Cu_2I_5$ framework is composed of $[Cu_2I_5]^{3-}$ clusters isolated by Cs^+ ions, where the clusters include two types of Cu^+ sites: a $[CuI_4]^{3-}$ tetrahedral site and a $[CuI_3]^{2-}$ plane triangle site that share an edge (Figure 2a). Moreover, the doped Zinc is in a tetrahedral coordination configuration,[20] demonstrating that the Zn^{2+} ion is capable of heterovalent substitution of the Cu^+ ion. X-ray photoelectron spectroscopy (XPS) analysis was conducted to demonstrate the valence state of Cu in the Zn^{2+}-doped $Cs_3Cu_2I_5$

NCs. The binding energies of 932.1 eV and 951.9 eV corresponded to Cu $2p_{3/2}$ and Cu $2p_{1/2}$, respectively, which were more similar to the Cu^{+} state than the Cu^{2+} state (Figure 2c). In addition, the characteristic satellite peak of Cu^{2+} (at approximately 943 eV) was not observed, which further excluded the presence of copper divalent in $Cs_3Cu_2I_5$ NCs. Two additional peaks in the ZnI_2 doped $Cs_3Cu_2I_5$ NCs appeared at 1022.3 and 1045.3 eV, which could be attributed to the Zn 2p, further demonstrating that Zn^{2+} ions were incorporated into $Cs_3Cu_2I_5$ NCs (Figure 2e). Compared with the non-doped $Cs_3Cu_2I_5$ NCs, the peak positions of Cs and I shifted to a decreased binding energy, which was due to the lower electronegativity of the Zn dopant element (as compared with Cu) (Figures. 2b, 2d). In the present case, the electron densities around the Cs and I atoms were increased, and their binding energies were decreased, indicating that the Zn element was successfully positioned in the $Cs_3Cu_2I_5$ NCs as an n-type dopant.

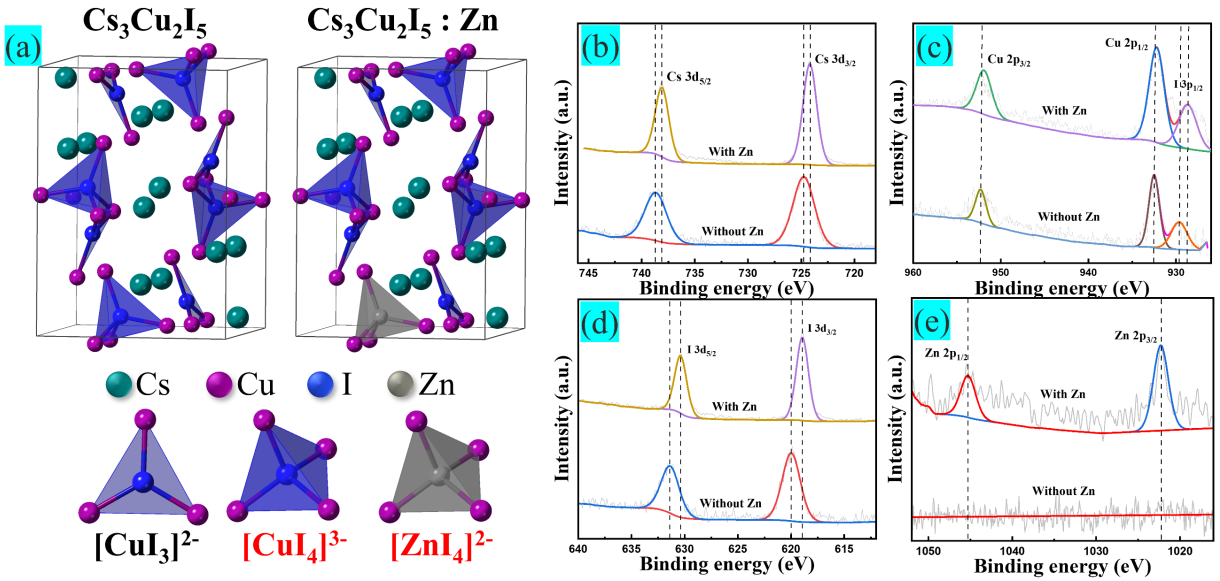

Figure 2. (a) Schematic crystal structure of the orthorhombic $Cs_3Cu_2I_5$ and Triclinic Cs_2ZnI_4. (b-e) High-resolution XPS spectrum of Cs ($3d_{5/2}$ and $3d_{3/2}$), Cu ($2p_{1/2}$ and $2p_{3/2}$), I ($3d_{3/2}$ and $3d_{5/2}$) and Zn ($2p_{1/2}$ and $2p_{3/2}$) of $Cs_3Cu_2I_5$ NCs synthesized with and without Zn, respectively.

Furthermore, we analyzed the luminescence properties of the Zn^{2+}-doped $Cs_3Cu_2I_5$ NCs using steady-state PL spectroscopy and UV-Vis absorption measurements. As shown in Figures. 3a and 3f, the sample exhibited good optical quality with a blue emission wavelength of approximately 440 nm and an FWHM of 73 nm. Such a broad emission spectrum originated from STE rather than being simply explained by a direct band emission.[21] STE can be viewed as an excited state defect that exists only when the material is excited.[16, 22] Its lattice distortion disappears with the termination of the excitation, while its energy relaxes to the ground state in the form of broadband luminescence.[23]

$Cs_3Cu_2I_5$ is a direct bandgap semiconductor.[4a] As can be seen in Figure 3b, the optical absorption edge of the non-doped $Cs_3Cu_2I_5$ is located at approximately 300 nm. The doping with Zn^{2+} effectively enhanced the ultraviolet absorption of $Cs_3Cu_2I_5$. The peak position was relatively red-shifted, indicating a decrease in its optical band gap value. As shown in the inset in Figure3b, the band gap that was estimated from the absorption spectra by the Tauc relation decreased from 4.13 eV to 4.10 eV, which was consistent with previous studies of Pb-based perovskites. [14] This indicated that the zinc dopant was more likely to exist in the intrinsic band gap in the form of impurity band gap states, which usually enhanced the optical absorption. These impurity gap states were shallow-level defects that did not hinder the electron transport. Owing to the defect tolerance of $Cs_3Cu_2I_5$, the shallow-level defects can broaden the radiative recombination path and increase the radiative recombination rate.[4b] Therefore, Zn^{2+} doping can improve the photoluminescence intensity of $Cs_3Cu_2I_5$.

We then performed PLQY measurements on the samples using an integrating sphere to quantify the PL intensity. For the ZnI_2 doped $Cs_3Cu_2I_5$ nanocrystals, the PLQY could be increased with an appropriate increase in the Cs/Cu feed ratio. The higher Cs/Cu feed ratio is, thus, an important factor leading to higher quantum yields. For the NCs solution, the dependence of PLQY on the Cs/Cu feed ratio is shown in Figure S7. The results show that the maximum obtained value was 92.8% for a Cs/Cu feed ratio of 4, and the corresponding PLQY measurement result is shown in Figure 3c. However, the highest PLQY was only 72.2% without the addition of ZnI_2 precursors, implying that Zn^{2+}-doped $Cs_3Cu_2I_5$ NCs were more favorable for the achievement of self-trapping exciton emission in a Cs-rich environment. These results differed from the studies of lead-based halide perovskites in that the excess of Cs precursors (Cs-oleate) in the system tended to trigger side reactions.[24]

The corresponding time-resolved PL (TRPL) decay curve of the sample with the best PL property was measured with a 290 nm excitation wavelength (as shown in Figure 3d). The resulting PL decay could be described by a bi-exponential fitting, and the PL lifetime of the Zn^{2+}-doped $Cs_3Cu_2I_5$ NCs was 3.7 μs, which was longer than that of the non-doped $Cs_3Cu_2I_5$ NCs (2.8 μs). Extended exciton lifetimes were an indication of a suppressed nonradiative recombination. In addition, the bi-exponential decay resulted in two-time constants: a longer lifetime assigned to NCs whose recombination is strongly mediated by surface impurities and traps, and a shorter lifetime caused by the intrinsic self-trapped exciton emission. The relative contribution of these two

terms to the PL emission in solution showed that the longer component had only a 3.3% contribution to the total PL emission, with a value of approximately 3.678 µs. The rest of the PL emission, i.e., 96.7%, was due to STE and the corresponding faster component lifetime was approximately 3.084 µs. The TRPL for NCs in the solution is shown in Table S2.

The lifetimes of $Cs_3Cu_2I_5$ NCs were fitted using bi-exponential decay kinetics (eq.1):

$$A(t) = A_1 e^{\left(\frac{-t}{\tau_1}\right)} + A_2 e^{\left(\frac{-t}{\tau_2}\right)} \quad (1)$$

Moreover, the average PL lifetimes (τ_{ave}) were calculated using eq.2.

$$\tau_{ave} = \frac{A_1\tau_1^2 + A_2\tau_2^2}{A_1\tau_1 + A_2\tau_2} \quad (2)$$

The origin of broadband emission was investigated by monitoring the PL excitation (PLE) spectra of Zn^{2+}-doped $Cs_3Cu_2I_5$ NCs at different wavelengths. The normalized PLE spectra showed the same shape and peak positions at different emission wavelengths from 390 to 490 nm (Figure 3e), suggesting that the broadband emission originated from the relaxation of the identical excited state.[25] Similarly, the normalized PL spectra exhibited the same characteristics when the excitation was varied from 270 to 320 nm (Figure 3f).

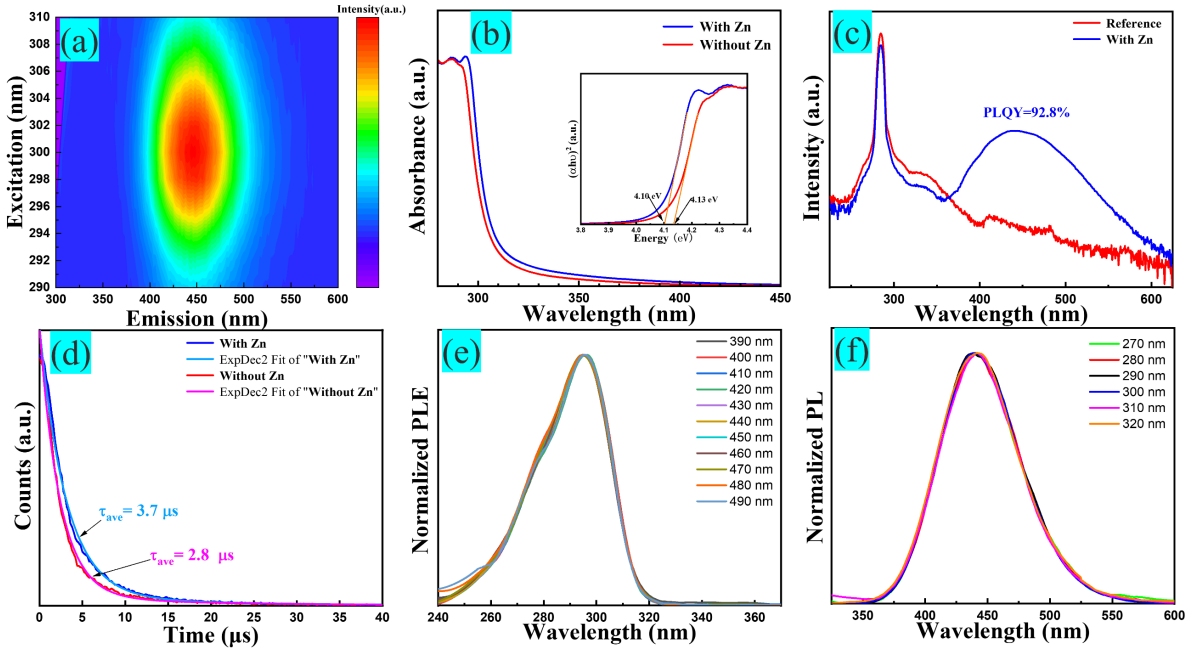

Figure 3. Luminescence performance of Zn^{2+}-doped $Cs_3Cu_2I_5$ NCs. (a) Excitation emission matrix plots of the Zn^{2+}-doped $Cs_3Cu_2I_5$ NCs. (b) The absorption spectrum and the corresponding Tauc plot shown in the inset. (c) PLQY results of the optimal Zn^{2+}-doped $Cs_3Cu_2I_5$ NCs under 290 nm excitation wavelength. (d) PL decay spectra of $Cs_3Cu_2I_5$ NCs with and without Zn. (e) PLE intensity under different emission wavelength from 390 to 490 nm of the Zn^{2+}-doped $Cs_3Cu_2I_5$ NCs. (f) PL intensity under different excitation wavelength from 270 to 320 nm of the Zn^{2+}-doped $Cs_3Cu_2I_5$ NCs.

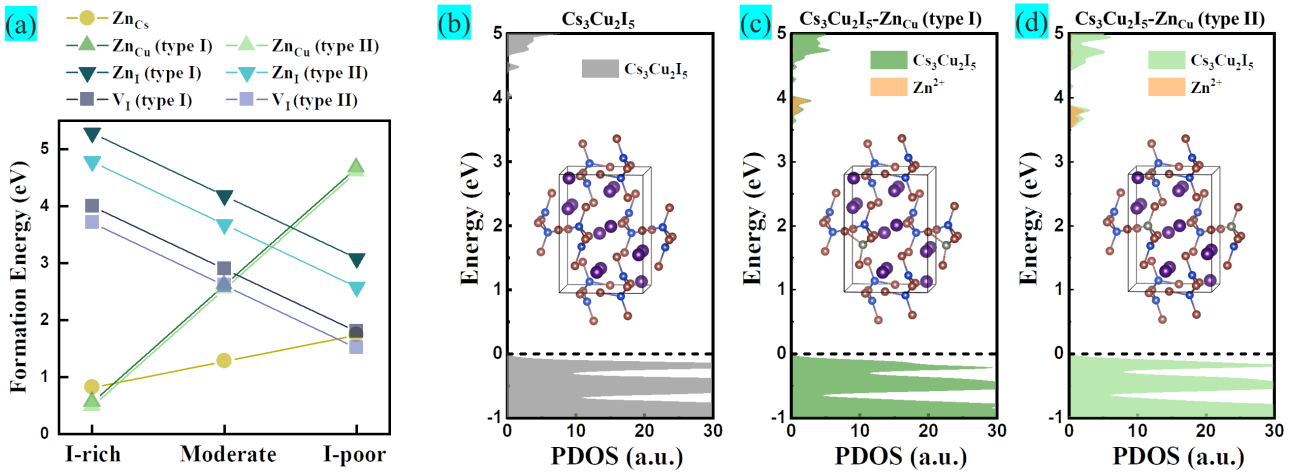

Figure 4. (a) Calculated defect formation energies for V_I (type I and II) and doping formation energies for Zn_{Cs}, Zn_{Cu} (type I and II), and Zn_I (type I and II) in $Cs_3Cu_2I_5$ at different growth conditions. Calculated projected density of states (PDOS) for (b) pristine $Cs_3Cu_2I_5$ and doped $Cs_3Cu_2I_5$ with (c) Zn_{Cu} (type I) and (d) Zn_{Cu} (type II). All the DFT calculations were performed at HSE06 level of theory. The insets illustrate the optimized crystal structures, and the valence band maximum is set at zero energy.

To understand the Zn^{2+}-doped effect on the improved optical properties of $Cs_3Cu_2I_5$ nanocrystals, we carried out density functional theory (DFT) calculations on the $Cs_3Cu_2I_5$ without and with a Zn dopant by using high-level HSE06 hybrid functional. We considered five intersite models, *i.e.*, Zn_{Cs}, two types of Zn_{Cu} (type I: three-coordinated Cu; type II: four-coordinated Cu), and two types of Zn_I (type I: two-coordinated I; type II: one-coordinated I). As shown in Figure S11, the optimized structure for the Zn_{Cu} unit (type I) has one $[CuI_4]^{3-}$ tetrahedral site and one $[ZnI_4]^{2-}$ tetrahedral site with a shared face. While the optimized structure for the Zn_{Cu} unit (type II) is similar to the pristine one, showing one $[ZnI_4]^{2-}$ tetrahedral site and one $[CuI_3]^{2-}$ planar triangular site with a shared edge. From the calculated doping formation energies (Figure 4), we find that, at the I-rich growth condition (*i.e.*, close to the experimental condition), both types of Zn_{Cu} have the smallest formation energy (~0.55 eV), suggesting that the Zn^{2+} dopant inclines to occupy Cu site. Meanwhile, the formation energies for the iodine vacancy (V_I) are much larger (3.7 and 4.0 eV), which would suppress the generation of V_I at the I-rich condition (note that V_I would give a deep trap state, as shown in Figure S12). Moreover, as compared to the pristine case, the Zn^{2+}-doped $Cs_3Cu_2I_5$ via Zn_{Cu} intersites would not introduce any deep trap states; instead, the shallow state appears below the valence band maximum (VBM) for both types of Zn_{Cu}, which can enrich the excited electron density at the band edge to enhance the self-trapped exciton emission. Similarly, for the case of Zn_{Cs} with a small formation (0.81 eV at the I-rich condition), we found that intersite Zn_{Cs} would introduce a shallow trap state above VBM (Figure S12).

Despite the remarkable photophysical properties of $Cs_3Cu_2I_5$ NCs, their poor stability has limited their practical applications, i.e., the luminescence of $Cs_3Cu_2I_5$ NCs decreased rapidly when exposed to atmospheric water vapor, and the colloidal solution precipitated quickly. The obtained Zn^{2+}-doped $Cs_3Cu_2I_5$ NCs were coated with a polymer to overcome these problems. Since EVA has good clarity, low-temperature toughness, stress-crack resistance, and excellent waterproof properties, we prepared a Zn^{2+}-doped $Cs_3Cu_2I_5$ NCs@EVA composite film at room temperature without tedious procedures, as shown in the schematic diagram of Figure 5a (see the experimental section for the details). XRD analysis confirmed the presence of the $Cs_3Cu_2I_5$ phase in the prepared composite film (Figure 5b). In addition, the Commission Internationale de l'Eclairage (CIE) chromaticity coordinate show that the composite film still retained the deep blue emission of the NCs (Figure S8).

As shown in Figure 5c, the NCs@EVA film displayed a water contact angle of approximately 100°, effectively preventing $Cs_3Cu_2I_5$ NCs from being in contact with water. Thus, the NC@EVA film was highly stable when exposed to water or water vapor. Moreover, the surface roughness of the Zn^{2+}-doped $Cs_3Cu_2I_5$ NCs@EVA composite film is 12.6 nm, (Figure 5d and Figure S9), which is similar to that of the pure EVA film (9.3 nm) and much lower than that of the undoped Zn^{2+} one (35.6 nm), indicating that Zn^{2+} doping is more conducive to the uniformity of the composite film surface. Furthermore, the photoluminescence quantum yield of the composite film with a thickness of 210 μm is 67.2% (Figure S13). The PL strength retention rate of the composite film remained at about 95% after 10 days of exposure to air (Figure S10), indicating that the crosslinked polymer network of EVA effectively prevented any leakage of NCs and provided additional protection to the NCs.

To further explore the PL emission mechanism of Zn^{2+}-doped $Cs_3Cu_2I_5$ NCs, we performed temperature-dependent PL measurements on the NCs@EVA composite films. Figure 5e shows the temperature-dependent PL pseudocolor map of the $Cs_3Cu_2I_5$ NCs@EVA composite film. Temperature-dependent exciton dynamic studies were performed to obtain the exciton binding energies (E_b) and to understand PL dynamics as a function of temperature for the $Cs_3Cu_2I_5$ NCs thin films. These observations were directly related to the absorption and emission of optoelectronic materials. The exciton binding energy of the Zn^{2+}-doped $Cs_3Cu_2I_5$ NCs was as large as 510 meV by fitting with eq.3 (Figure 5f).

$$I(T) = \frac{I_0}{1 + Ae^{-E_b/k_BT}} \quad (3)$$

where I_0 is the integrated PL intensity at 0 K, A is the proportional coefficient, and k_B is the Boltzmann constant.

For metal halide perovskites, their exciton binding energies are generally in the order of tens of meV, which is much lower than that of organic materials. Based on polycrystalline perovskite films, the small exciton binding energy makes the excitons less stable in electroluminescent devices. In the present work, the surface states of the Zn^{2+}-doped nanocrystals had a larger exciton binding energy as compared with the previously reported intrinsic nanocrystals,[5c, 26] which could effectively enhance the excitation-acoustic coupling. It also resulted a higher radiative transition probability. This dramatic increase in exciton binding energy may be responsible for the high PLQY after doping.

To investigate the degree of electron-phonon coupling, the Huang-Rhys factor, *S,* and phonon frequency, $\hbar\omega_{phonon}$, were obtained by fitting a function of the inverse of the FWHM temperature (Figure5g). The Huang-Rhys equation is presented in eq.4.

$$FHWM = 2.36\sqrt{S}\,\hbar\omega_{phonon}\sqrt{\coth\frac{\hbar\omega_{phonon}}{2k_BT}} \quad (4)$$

The fitted results of the S factor and $\hbar\omega_{phonon}$ were 10 and 57 meV, respectively. Notably, the S-factor was much higher than those of the Pb-based perovskites with band-edge luminescence characteristics,[27] indicating stronger electron-phonon coupling interactions in $Cs_3Cu_2I_5$ NCs, and the value of $\hbar\omega_{phonon}$ was very close to those of all-inorganic perovskites.[28]

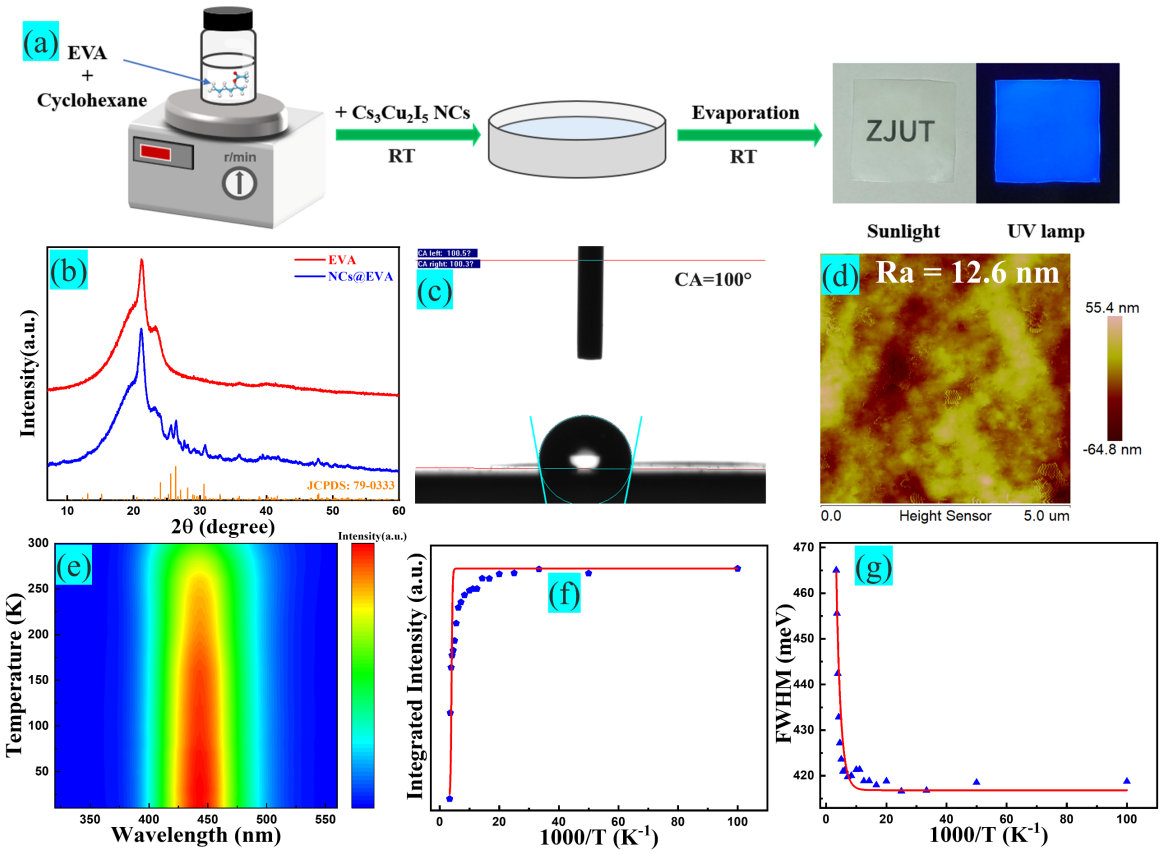

Figure 5. (a) Schematic diagram for synthesis of Zn^{2+}-doped $Cs_3Cu_2I_5$ NCs@EVA composite film. (b) XRD patterns of pure EVA film and Zn^{2+}-doped $Cs_3Cu_2I_5$ NCs@EVA composite film. (c) Water contact-angle measurement of Zn^{2+}-doped $Cs_3Cu_2I_5$ NCs@EVA composite film. (d) AFM micrographs of prepared Zn^{2+}-doped $Cs_3Cu_2I_5$ NCs@EVA composite films. (e) Pseudocolor map of temperature-dependent PL spectra of Zn^{2+}-doped $Cs_3Cu_2I_5$ NCs@EVA composite film, ranging from 10 to 300 K. (f) Fitting curve of the integrated PL intensity and (g) fwhm as a function of reciprocal temperature.

To demonstrate the potential application of composite films in X-ray scintillation, we evaluated the X-ray imaging performance of the scintillator films by using an X-ray imaging system (Figure 6a). We first plotted the radioluminescence (RL) spectra of the composite films under X-ray excitation, as shown in Figure 6b. The films exhibited dark blue RL, indicating that the prepared films had good RL properties. Figure 6c, with its inset, reflect the RL intensity variation of $Cs_3Cu_2I_5$ under excitation at low and high dose rates of X-rays, respectively. Both show a good linear response of the RL intensity to the X-ray dose rate. The stability of the composite film was also explored, as shown in Figure S14. Under 60 min of continuous X-ray irradiation (at a dose rate of 0.2 mGy_{air} s^{-1}), the intensity of RL exhibited small fluctuations, demonstrating that the film has good stability under X-ray. The detection limit of the composite films was calculated to be 0.31 μGy_{air} s^{-1} at a signal-to-noise ratio of 3, which was about 18 times lower than the dose of standard medical examinations (5.5 μGy_{air} s^{-1}). In addition, the spatial resolution of the X-ray imaging was estimated to be 14-16 lp/mm, as shown in Figure 6d, using a standard lead X-ray resolution line-pair card. Detailed X-ray images, with a high spatial resolution of 15.7 lp/mm, could be achieved when the modulation transfer function (MTF) was 0.2. (Figure 6e). This imaging system based on an NCs@EVA film scintillation screen with a thickness of 210 μm was used to validate the evaluated spatial resolution of X-ray imaging. As shown in Figure 6f,g, the internal structure of a ballpoint pen and the skeleton of a small fish could be revealed in detail, indicating the great potential of the NCs@EVA film screen for bioimaging detection.

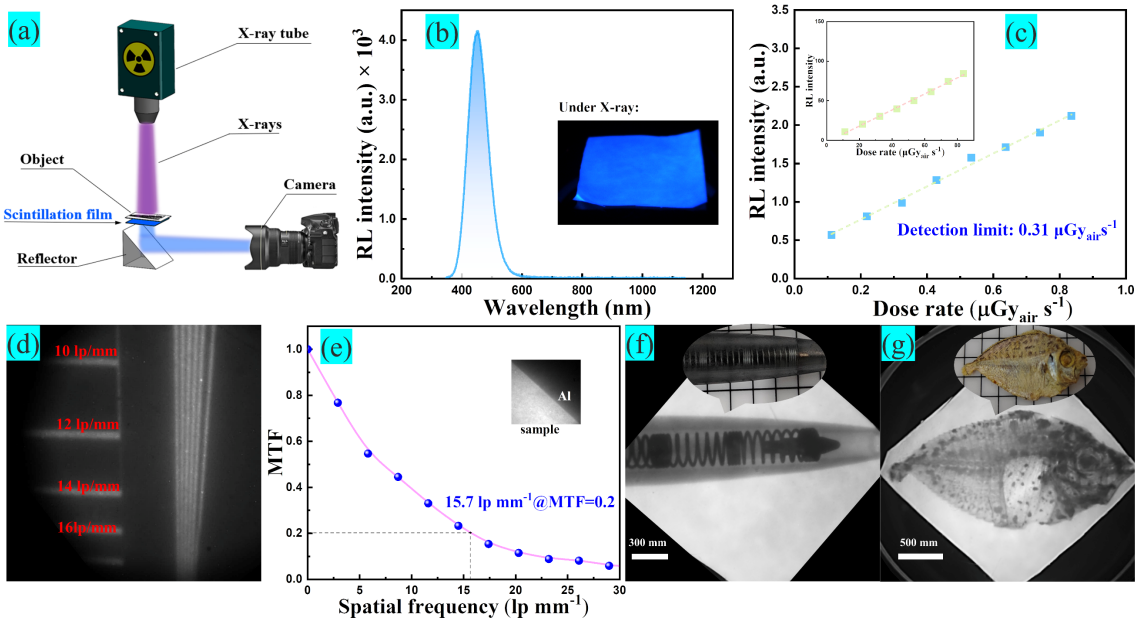

Figure 6. (a) Schematic diagram of the X-ray imaging system. (b) RL spectra of the Zn^{2+}-doped $Cs_3Cu_2I_5$ NCs@EVA composite film, and the X-ray photographs of the film is shown in the inset. (c) RL intensity of scintillator films as a function of dose rate and their detection limit. (d) Images of the line-pair card under X-ray radiation. (e) X-ray imaging of scintillator film on standard resolution card and MTF calculation of the scintillator film. (f, g) Photographs of (f) ballpoint pen and (g) fish and X-ray images captured by NCs@EVA film.

Conclusion

In conclusion, we reported a strategy to control the size morphology of $Cs_3Cu_2I_5$ NCs by tuning the growth kinetic equilibrium using Zn^{2+} doping. Monodisperse $Cs_3Cu_2I_5$ nanocubes with dark blue emission and a maximum PLQY of 92.8% were obtained. The DFT results on the doping formation energies suggest that the Zn^{2+} dopant would occupy Cu site that can enrich the excited electron density at the band-edge for enhancing the STE emission of $Cs_3Cu_2I_5$. Meanwhile, at the I-rich condition, the formation of I vacancy is significantly suppressed, which can reduce the nonradiative centers induced by I vacancy. Based on Zn^{2+}-doped $Cs_3Cu_2I_5$ NCs@EVA composite films, flexible X-ray scintillator films with environmentally friendly and excellent luminescence properties can be prepared with a spatial resolution of up to 15.7 lp/mm. These advantages show the promising potential of the Zn^{2+} doping strategy for high luminescence performance and environmentally friendly X-ray detector applications.

Acknowledgements

This work was supported by the National Key Research and Development Project of China (2022YFE0113800), National Natural Science Foundation of China (Grant Nos. 52172160 and 21805181), Leading Innovative and Entrepreneur Team Introduction Program of Zhejiang (2020R01002), and Fundamental Research Funds for the Provincial Universities of Zhejiang (RF-C2022005). J.Y. acknowledges financial support from the Hong Kong Polytechnic University (grant P0042930).

Keywords: Cesium copper halide • Doping • nanocrystal • composite film • X-ray imaging

References

[1] a) T. He, Y. Zhou, X. Wang, J. Yin, L. Gutiérrez-Arzaluz, J.-X. Wang, Y. Zhang, O. M. Bakr, O. F. Mohammed, *ACS Energy Lett.* **2022**, *7*, 2753-2760; b) L. Lu, M. Sun, T. Wu, Q. Lu, B. Chen, B. Huang, *Nanoscale Adv.* **2022**, *4*, 680-696; c) K. Xia, P. Ran, W. Wang, J. Yu, G. Xu, K. Wang, X. Pi, Q. He, Y. Yang, J. Pan, *Adv. Opt. Mater.* **2022**, *10*, 2201028.

[2] a) Z. Pan, L. Wu, J. Jiang, L. Shen, K. Yao, *J. Phys. Chem. Lett.* **2022**, *13*, 2851-2861; b) J. Wu, L. Wang, A. Feng, S. Yang, N. Li, X. Jiang, N. Liu, S. Xie, X. Guo, Y. Fang, Z. Chen, D. Yang, X. Tao, *Adv. Funct. Mater.* **2021**, *32*, 2109149; c) J. Di, H. Li, J. Su, H. Yuan, Z. Lin, K. Zhao, J. Chang, Y. Hao, *Adv. Sci.* **2022**, *9*, e2103482; d) Z. Zhang, H. Dierks, N. Lamers, C. Sun, K. Novakova, C. Hetherington, I. G. Scheblykin, J. Wallentin, *ACS Appl. Nano Mater.* **2022**, *5*, 881-889; e) J. Peng, C. Q. Xia, Y. Xu, R. Li, L. Cui, J. K. Clegg, L. M. Herz, M. B. Johnston, Q. Lin, *Nat. Commun.* **2021**, *12*, 1531; f) J. Hui, P. Ran, Y. Su, L. Yang, X. Xu, T. Liu, Y. M. Yang, *J. Phys. Chem. C* **2022**, *126*, 12882-12888.

[3] a) L. Lian, M. Zheng, P. Zhang, Z. Zheng, K. Du, W. Lei, J. Gao, G. Niu, D. Zhang, T. Zhai, S. Jin, J. Tang, X. Zhang, J. Zhang, *Chem. Mater.* **2020**, *32*, 3462-3468; b) L. Han, B. Sun, C. Guo, G. Peng, H. Chen, Z. Yang, N. Li, Z. Ci, Z. Jin, *Adv. Opt. Mater.* **2022**, *10*, 2102453; c) H. Chen, J. M. Pina, F. Yuan, A. Johnston, D. Ma, B. Chen, Z. Li, A. Dumont, X. Li, Y. Liu, S. Hoogland, Z. Zajacz, Z. Lu, E. H. Sargent, *J. Phys. Chem. Lett.* **2020**, *11*, 4326-4330.

[4] a) Y. Hui, S. Chen, R. Lin, W. Zheng, F. Huang, *Mater. Chem. Front.* **2021**, *5*, 7088-7107; b) Y. Yin, Y. Wang, Q. Sun, Y. Yang, Y. Wang, Z. Yang, W. J. Yin, *J. Phys. Chem. Lett.* **2022**, *13*, 4177-4183; c) F. Zeng, Y. Guo, W. Hu, Y. Tan, X. Zhang, J. Feng, X. Tang, *ACS Appl. Mater. Interfaces* **2020**, *12*, 23094-23101; d) X. Li, J. Chen, D. Yang, X. Chen, D. Geng, L. Jiang, Y. Wu, C. Meng, H. Zeng, *Nat. Commun.* **2021**, *12*, 3879.

[5] a) L. Xie, B. Chen, F. Zhang, Z. Zhao, T. Jiang, M. Wang, Y. Wu, L. Huang, W. Song, Y. Liu, Y. Wang, *J. Lumin.* **2021**, *239*, 118333; b) Z. Ma, Z. Shi, D. Yang, Y. Li, F. Zhang, L. Wang, X.

Chen, D. Wu, Y. Tian, Y. Zhang, L. Zhang, X. Li, C. Shan, *Adv. Mater.* **2021**, *33*, e2001367; c) L. Wang, Z. Shi, Z. Ma, D. Yang, F. Zhang, X. Ji, M. Wang, X. Chen, G. Na, S. Chen, D. Wu, Y. Zhang, X. Li, L. Zhang, C. Shan, *Nano Lett.* **2020**, *20*, 3568-3576.

[6] Z. X. Zhang, C. Li, Y. Lu, X. W. Tong, F. X. Liang, X. Y. Zhao, D. Wu, C. Xie, L. B. Luo, *J. Phys. Chem. Lett.* **2019**, *10*, 5343-5350.

[7] a) F. Cao, X. Xu, D. Yu, H. Zeng, *Nanophotonics* **2021**, *10*, 2221-2247; b) J. Zhou, K. An, P. He, J. Yang, C. Zhou, Y. Luo, W. Kang, W. Hu, P. Feng, M. Zhou, X. Tang, *Adv. Opt. Mater.* **2021**, *9*, 2002144.

[8] a) N. Zhang, K. Xia, Q. He, J. Pan, *ACS Mater. Lett.* **2022**, *4*, 1233-1254; b) W. Cui, J. Zhao, L. Wang, P. Lv, X. Li, Z. Yin, C. Yang, A. Tang, *J. Phys. Chem. Lett.* **2022**, *13*, 4856-4863.

[9] a) Y.-H. Cheng, R. Suzuki, N. Shinotsuka, H. Ebe, N. Oshita, R. Yamakado, T. Chiba, A. Masuhara, J. Kido, *Sci. Rep.* **2022**, *12*, 1-8; b) C.-X. Li, S.-B. Cho, D.-H. Kim, I.-K. Park, *Chem. Mater.* **2022**, *34*, 6921-6932.

[10] a) Y. Li, P. Vashishtha, Z. Zhou, Z. Li, S. B. Shivarudraiah, C. Ma, J. Liu, K. S. Wong, H. Su, J. E. Halpert, *Chem. Mater.* **2020**, *32*, 5515-5524; b) X. Huang, Q. Sun, B. Devakumar, *Mater. Today Chem.* **2020**, *17*, 100288; c) F. Zhang, Z. Zhao, B. Chen, H. Zheng, L. Huang, Y. Liu, Y. Wang, A. L. Rogach, *Adv. Opt. Mater.* **2020**, *8*, 1901723.

[11] Y. Chen, H. Yang, J. Song, B. Zhang, *J. Mater. Chem. C* **2022**, *10*, 5147-5154.

[12] A. Liu, H. Zhu, W. T. Park, S. J. Kim, H. Kim, M. G. Kim, Y. Y. Noh, *Nat. Commun.* **2020**, *11*, 4309.

[13] a) F. Gao, X. Zhu, Q. Feng, W. Zhong, W. Liu, H. Xu, Y. Liu, *Nano Energy* **2022**, *98*, 107270; b) X. Hu, P. Yan, P. Ran, L. Lu, J. Leng, Y. M. Yang, X. Li, *J. Phys. Chem. Lett.* **2022**, *13*, 2862-2870; c) J. Qu, S. Xu, Y. Cui, C. Wang, *Chem. Eur. J.* **2022**, *28*, e202200877; d) L. Stand, D. Rutstrom, M. Koschan, M.-H. Du, C. Melcher, U. Shirwadkar, J. Glodo, E. Van Loef, K. Shah, M. Zhuravleva, *Nucl. Instrum. Methods Phys. Res. A* **2021**, *991*, 164963; e) Q. Wang, Q. Zhou, M. Nikl, J. Xiao, R. Kucerkova, A. Beitlerova, V. Babin, P. Prusa, V. Linhart, J. Wang, X. Wen, G. Niu, J. Tang, G. Ren, Y. Wu, *Adv. Opt. Mater.* **2022**, *10*, 2200304.

[14] Y. Guo, J. Su, L. Wang, Z. Lin, Y. Hao, J. Chang, *J. Phys. Chem. Lett.* **2021**, *12*, 3393-3400.

[15] L. Protesescu, S. Yakunin, M. I. Bodnarchuk, F. Krieg, R. Caputo, C. H. Hendon, R. X. Yang, A. Walsh, M. V. Kovalenko, *Nano Lett.* **2015**, *15*, 3692-3696.

[16] Z. Ma, Z. Shi, C. Qin, M. Cui, D. Yang, X. Wang, L. Wang, X. Ji, X. Chen, J. Sun, D. Wu, Y. Zhang, X. J. Li, L. Zhang, C. Shan, *ACS Nano* **2020**, *14*, 4475-4486.

[17] S. K. Sharma, S. Mamgain, B. Attarwala, A. Yella, *Nanoscale Adv.* **2019**, *1*, 2502-2509.

[18] Y. Lu, G. Li, S. Fu, S. Fang, L. Li, *ACS Omega* **2021**, *6*, 544-552.

[19] F. Zhang, W. Liang, L. Wang, Z. Ma, X. Ji, M. Wang, Y. Wang, X. Chen, D. Wu, X. Li, Y. Zhang, C. Shan, Z. Shi, *Adv. Funct. Mater.* **2021**, *31*, 2105771.

[20] P. Cheng, L. Feng, Y. Liu, D. Zheng, Y. Sang, W. Zhao, Y. Yang, S. Yang, D. Wei, G. Wang, K. Han, *Angew. Chem. Int. Ed.* **2020**, *59*, 21414-21418.

[21] B. Zhang, X. Wu, S. Zhou, G. Liang, Q. Hu, *Front. Optoelectron.* **2021**, *14*, 459-472.

[22] S. Li, J. Luo, J. Liu, J. Tang, *J. Phys. Chem. Lett.* **2019**, *10*, 1999-2007

[23] M. D. Smith, B. A. Connor, H. I. Karunadasa, *Chem. Rev.* **2019**, *119*, 3104-3139.

[24] Y. Qian, Y. Shi, G. Shi, G. Shi, X. Zhang, L. Yuan, Q. Zhong, Y. Liu, Y. Wang, X. Ling, F. Li, M. Cao, S. Li, Q. Zhang, Z. Liu, W. Ma, *Solar RRL* **2021**.

[25] P. Cheng, L. Sun, L. Feng, S. Yang, Y. Yang, D. Zheng, Y. Zhao, Y. Sang, R. Zhang, D. Wei, W. Deng, K. Han, *Angew. Chem. Int. Ed.* **2019**, *58*, 16087-16091.

[26] L. Lian, M. Zheng, W. Zhang, L. Yin, X. Du, P. Zhang, X. Zhang, J. Gao, D. Zhang, L. Gao, G. Niu, H. Song, R. Chen, X. Lan, J. Tang, J. Zhang, *Adv. Sci.* **2020**, *7*, 2000195.

[27] X. Lao, Z. Yang, Z. Su, Z. Wang, H. Ye, M. Wang, X. Yao, S. Xu, *Nanoscale* **2018**, *10*, 9949-9956.

[28] J. Zhang, Y. Yang, H. Deng, U. Farooq, X. Yang, J. Khan, J. Tang, H. Song, *ACS Nano* **2017**, *11*, 9294-9302.